Representing the effects of giant aerosol in droplet nucleation in E3SMv2

Yu Yao[1], Po-Lun Ma[1], Yi Qin[1], Matthew W. Christensen[1], Hui Wan[1], Kai Zhang[1], Balwinder Singh[1], Meng Huang[1], and Mikhail Ovchinnikov[1]

[1]Atmospheric, Climate, and Earth Sciences Division, Pacific Northwest National Laboratory, Richland, WA, USA

Correspondence: Yu Yao (yu.yao@pnnl.gov)

Abstract. Giant aerosol, i.e., those with diameters larger than 1 μm, can form large droplets via condensational growth to sizes similar to drizzle particles without being activated. In this study, we assess the impacts of giant aerosol on clouds, precipitation, and radiation when activated giant aerosol are directly categorized as raindrops using the U.S. Department of Energy's Energy Exascale Earth System Model version 2 (E3SMv2). We find that categorizing activated giant aerosol as raindrops reduces cloud liquid water path by 11.38% globally, with most pronounced reduction in the mid-latitudes. We also find that this approach improves model's ability to simulate the positive correlation between surface rain rate and coarse mode aerosol concentration in regions of low precipitation. The effective radiative forcing associated with aerosol-cloud interactions (ERFaci) reduces from –1.37 to between –0.94 and –1.23 W m^{-2}, depending on the size of giant aerosol. Our results highlight the importance of a better representation of giant aerosol in Earth system models to provide better predictions of cloud, precipitation, and the climate.

1 Introduction

Aerosol-cloud interactions (ACI) remain a large source of uncertainty in Earth system modeling. The latest estimates of effective radiative forcing associated with ACI (ERFaci) range between –1.73 and –0.27 W m^{-2} (16–84% likelihood) (Bellouin et al., 2020). Aerosol impacts on liquid clouds lead to significant changes in the Earth's energy balance (Lohmann and Feichter, 2005; Platnick et al., 2016; Quaas and Gryspeerdt, 2022) and are characterized as the cloud albedo effect (Twomey, 1977) and cloud lifetime effect (Albrecht, 1989). Despite decades of active research, the relationship between cloud droplet number concentration (N_{d}) and aerosol number concentration, as well as the correlation between droplet number concentration and cloud liquid water path, remains poorly understood and differs between models and observations (Gryspeerdt et al., 2014; Grosvenor et al., 2017; Gryspeerdt et al., 2019; Varble et al., 2023). The properties of aerosol particles, including size and chemical composition, affect their potential to act as cloud condensation nuclei (CCN)(Petters and Kreidenweis, 2007; Riemer et al., 2019). However, it's the size of the aerosols that holds greater significance than their chemical composition in determining this ability (Dusek et al., 2006). Giant aerosol (GA) particles that are larger than 1 μm in dry diameter can affect clouds and warm rain formation (Feingold et al., 1999; Jensen and Lee, 2008).

Sea salt and dust aerosol are two of the common natural GA types. Soluble sea salt particles are efficient cloud condensation
25 nuclei (CCN), whereas insoluble dust particles are crucial for ice cloud formation (Froyd et al., 2022). Understanding the
impact of giant particles remains challenging from both observation and numerical model perspectives. It is hard to measure
these large particles as their number concentrations are typically several orders of magnitude lower than those of fine particles.
For example, in a recent field campaign over northeast Pacific and northwest Atlantic, the number concentration of GA with dry
diameter larger than 2 μm is reported to be in the order of 10^{-1} cm^{-3} (Gonzalez et al., 2022), while the CCN at supersaturation
30 of 0.4% over Northern Hemisphere mid-latitude is in the order of 10^{2} cm^{-3} (Yu and Luo, 2009). The microphysical processes
associated with GA are different from those with fine aerosol. Because of their large critical size, the activation of GA is subject
to kinetic limitations, one of which being the inertial mechanism. This mechanism implies large particles can not reach critical
diameter in a limited timescale and they stay interstitial during cloud formation processes (Nenes et al., 2001).

The impacts of GA on warm rain processes remain highly uncertain and is an active research area. Nenes and Seinfeld (2003)
35 came up with the population-splitting framework to describe the growth of activated aerosol populations using two different
groups: smaller particles following the equilibrium growth, while larger particles are dominant by condensational growth after
reaching critical supersaturation. Barahona et al. (2010) revised the growth rates for those inertially-limited larger particles in
the population-splitting method to reduce the overestimation of cloud droplets number concentration when there is a significant
portion of large CCN. A more accurate representation of droplets growth in the cases where inertially-limited particles are the
40 dominant CCN are proposed by Morales Betancourt and Nenes (2014). However, these population-splitting works were based
on the assumptions that the the effects of curvature and solutes on the equilibrium vapor pressure of the growing droplets are
ignored. Jensen and Nugent (2017) found that accounting for solute effects in the condensational growth of GA particles is
crucial, enabling them to reach drizzle size within tens of minutes only by condensation. Earlier studies also noticed that GA
can expedite warm rain initiation through an enhancement of the collision-coalescence process (Yin et al., 2000; Lasher-Trapp
45 et al., 2001). Using a large eddy simulation (LES), Cheng et al. (2009) showed that GA impacts on precipitation rate are more
significant in a polluted environment. However, other studies reported that GA only had limited effects on warm rain through
condensational growth (Zhang et al., 2006; Blyth et al., 2013).

It is computationally challenging to incorporate detailed microphysical processes that GA go through in Earth system models
(ESMs). Therefore, parameterizations have been developed to "short circuit" the actual coalescence process so that the effects,
50 rather than the processes, are represented in ESMs (Mechem and Kogan, 2008; Posselt and Lohmann, 2008). In Posselt and
Lohmann (2008), a giant CCN (GCCN) parameterization was implemented in ECHAM5. They calculated the GCCN effects
by diagnosing large activated particles with size larger than 5 or 10 um and categorizing them as rain droplets. However,
the activation of these GA particles in the work followed the same process as other smaller particles, neglecting the kinetic
limitations. To the extent of our knowledge, there has not been any study that addresses both the kinetic limitations and
55 condensation growth of giant particles at global scale. In this study, we assess the impacts of GA using the U.S. Department of
Energy's Energy Exascale Earth System Model version 2 (E3SMv2) (Golaz et al., 2022). We assess the impacts of the inertial
mechanism in E3SMv2 by prohibiting GA from activation into cloud droplets. Furthermore, following the approach of Posselt
and Lohmann (2008), we categorize the activated GA as rain droplets rather than cloud droplets to reflect their large critical

size. Our results show that GA play an important role on cloud, precipitation, and ERFaci. This manuscript is organized as follows. Model description is provided in section 2. Effects of GCCN on liquid cloud and rain are presented in section 3. The changes in simulated precipitation susceptibility to aerosol and radiative forcing are included in section 4 and 5, respectively. Discussion and conclusions are given in section 6.

2 Methodology

2.1 Model description

We use E3SMv2 (Golaz et al., 2022) in this study. The atmosphere model in E3SMv2 is based on the E3SM atmosphere model version 1 (Rasch et al., 2019) with some improvements as described below. Compared to E3SMv1 (Golaz et al., 2019), E3SMv2 speeds up the simulations by using separate grids for dynamicss and physics (Hannah et al., 2021). E3SMv2 uses the Cloud Layers Unified By Binormals (CLUBB) parameterization (Golaz et al., 2002, 2022) for turbulence, shallow cumulus, and cloud macrophysics. The updated Zhang and McFarlane (1995) deep convection scheme (hereinafter ZM) in E3SMv2 uses a new convection trigger (Xie et al., 2019) that improves the simulated diurnal cycle of precipitation. A two-moment bulk cloud microphysics scheme (Gettelman and Morrison, 2015) (hereinafter MG2) is used to represent cloud microphysics. The 4-mode version of Modal Aerosol Module (MAM4; Liu et al. (2016)) with updates is used in E3SMv2 (Wang et al., 2020). Substantial model calibration in convection, cloud, and subgrid effects (Ma et al., 2022) is included in E3SMv2 to improve the simulation fidelity.

Assessing the impacts of GA requires a realistic representation of the life cycle of coarse mode aerosol, which is affected not only by the physical representation but also by the numerical discretization method used in the model. In E3SMv2, aerosol dry removal processes (i.e., gravitational settling and turbulent dry deposition) is calculated immediately after the surface emission fluxes are applied and before turbulent mixing is considered. Wan et al. (2023) and Vogl et al. (2023) showed that this sequence of calculation leads to overestimated dry removal and contributes to the overly strong dust removal in E3SMv1 pointed out by Feng et al. (2022). This could also lead to unrealistically low GA concentration in the atmosphere, because large particles are more susceptible to dry removal. In order to reduce the numerical error with a minimal amount of code modification, Wan et al. (2023) proposed to move the application of surface emissions to right before the turbulent mixing of aerosols to provide a tighter numerical coupling of these processes and discussed the impacts on the simulated total mass of interstitial dust aerosol in E3SMv1. This change has been incorporated in E3SMv2 used for this work.

2.2 Representing giant aerosol in aerosol activation

The Abdul-Razzak and Ghan (2000) scheme is used in E3SMv2 to represent aerosol activation. The parameterization computes the maximum supersaturation and activation fraction as a function of aerosol size, hygroscopicity, and number concentration in each mode i, and relative humidity, temperature, pressure, and updraft velocity. The aerosol module MAM4 in E3SMv2 represents aerosol population using four lognormal distributions:Aitken, accumulation, coarse and primary-carbon modes. For

each mode, activated fraction f_i, activated number n_i and activated mass m_i in a rising air parcel with maximum supersaturation $S_{\max}$ are calculated as:

$$f_i = (\frac{S_i}{S_{\max}})^{\frac{2}{3}}, \tag{1}$$

$$n_i = N_i \frac{1}{2}[1 - \mathrm{erf}(u_i)], \tag{2}$$

$$m_i = M_i \frac{1}{2}[1 - \mathrm{erf}(u_i - \frac{3\sqrt{2}}{2}\ln\sigma_i)], \tag{3}$$

where S_i, σ_i, N_i, M_i are the critical supersaturation, geometric standard deviation of aerosol size distribution, total number concentration and total mass concentration of mode i, respectively. The u_i is calculated as:

$$u_i = \frac{f_i}{\sqrt{2}\ln_{\sigma_i}}. \tag{4}$$

The activated aerosol are tracked as cloud-borne aerosol in MAM4. The time tendency of cloud-borne aerosol number concentration due to aerosol activation is the same as that of cloud droplet number N_c.

To consider the kinetic limitation of GA, we remove the coarse mode aerosol with dry diameters large than a certain threshold size from the activation calculation (green box in Fig. 1). There isn't a precise size definition for the largeness of GA, and we'll assess their effects by using various thresholds. Three threshold sizes were tested: 2, 3 and 4 um. Removing GA from the activation calculation prevents them from condensational growth and eventual activation as cloud droplets, allowing more fine aerosol in the Aitken and accumulation modes to be activated. In reality, GA can still grow through condensation even though most of them will not grow to their critical sizes within a model timestep. Therefore, this treatment that does not allow GA to grow can be considered as the upper limit of the inertial effect. In Section 3, we show that the inertial effect of GA is negligible in E3SMv2.

Next, we consider the fact that even though GA do not grow to their critical sizes, they can grow to the drizzle size without being activated. To "short circuit" the coalescence process, we adopt the Posselt and Lohmann (2008) approach that treats the GCCN as rain droplets with some modifications so that the parameterization works within MAM4: First, we assume that GA is activated at the same fraction of the coarse-mode aerosol, even though they are not part of the activation calculation as described above. Then, we diagnose the GCCN number from the coarse-mode cloud-borne aerosol with diameters larger than a threshold within the same time step, as shown in the red box in Fig 1. Same as the value used in the kinetic limitation treatment, here we use 2, 3 and 4 μm as the threshold. While in the default model, the total cloud-borne aerosol number tendency from aerosol activation is the source term for cloud droplet number, the new treatment applies the GCCN part of the number tendency to increase rain number. Rain mass tendency from GCCN is then calculated based on the assumed size of 25 μm, which is the initial rain droplet size assumed in the model. The rain mass associated with GCCN is converted from liquid cloud.
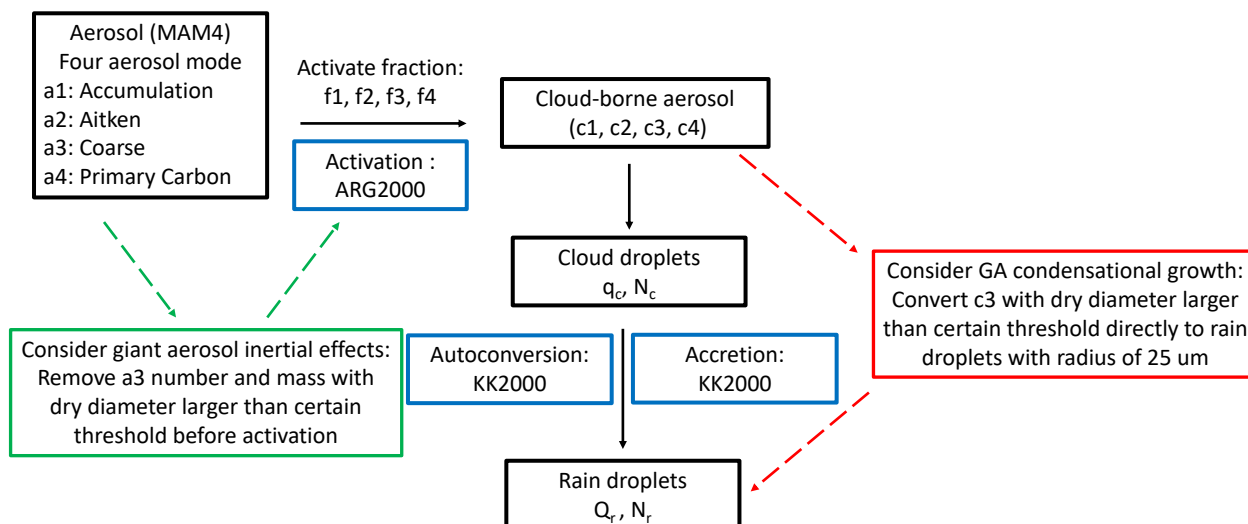
Figure 1. Model framework to consider GA effects in E3SMv2. Processes in the blue boxes are the default microphysical processes aerosols involved to form rain droplets. Process in green box is the treatment to consider GA inertial effects and stay interstitial. Process in the red box is the treatment to consider GA condensational growth by categorizing the GCCN to drizzle droplets.

2.3 Experiments setup

120 We conduct two sets of simulations: One group consists of 11-year free-running simulations with the last 10 years used for analysis; the other group consists of 2-year simulations with winds nudged to MERRA reanalysis (Sun et al., 2019) with year 2 used for analysis. The first group of simulations are with monthly output data and used for climatology analysis. Unless specifically noted, all the analyses are based the 10-year climatology. The second group of simulations has hourly output to facilitate model evaluation against observations. All simulations used the resolution of approximately 1° with 72 vertical

125 layers. In each group, we conducted a default E3SMv2 model simulation (Ctrl) and 6 experiments, testing the GA inertial effects and the GCCN effects at 3 different size thresholds. The free-running simulations were done with present-day (PD) and pre-industrial (PI) aerosol emissions for radiative forcing calculations. Table 1 summarizes the experiments.

Table 1. E3SMv2 simulation cases

Type	Emission	Cases	GCCN diameter	Giant aerosol treatment
free-running, 6 years, monthly	PD/PI	Ctrl	–	–
		GA_inert_D2	2 µm	Not activate
		GA_inert_D3	3 µm	Not activate
		GA_inert_D4	4 µm	Not activate
		GCCN_D2	2 µm	Convert to rain
		GCCN_D3	3 µm	Convert to rain
		GCCN_D4	4 µm	Convert to rain
nudging, 2 years, hourly	PD	Ctrl	–	–
		GA_inert_D2	2 µm	Not activate
		GA_inert_D3	3 µm	Not activate
		GA_inert_D4	4 µm	Not activate
		GCCN_D2	2 µm	Convert to rain
		GCCN_D3	3 µm	Convert to rain
		GCCN_D4	4 µm	Convert to rain

3 Effects of giant aerosol on cloud and precipitation

We first assess the fraction of GA and GCCN in the coarse mode. In the original MAM implemented in the Community
Atmosphere Model version 5 (CAM5), the global annual mean coarse mode diameter 10th and 90th percentiles are 0.8 and
3.65 um, respectively, with geometric standard deviation (σ_{g}) of 1.8 (Liu et al., 2012). The cumulative distribution function of
the number concentration CDF_N and total volume CDF_V are:

$$\mathrm{CDF}_N = \frac{1}{2}(1 + \mathrm{erf}(\frac{\ln(D_{\mathrm{GA}}/D_{\mathrm{mean}})}{\sqrt{2}\ln\sigma_{\mathrm{g}}})), \tag{5}$$

$$\mathrm{CDF}_V = \frac{1}{2}\mathrm{erfc}(\frac{3}{2}\sqrt{2}\ln\sigma_{\mathrm{g}} - \frac{\ln(D_{\mathrm{GA}}/D_{\mathrm{mean}})}{\sqrt{2}\ln\sigma_{\mathrm{g}}}), \tag{6}$$

where D_{GA} is the GA threshold and D_{mean} is the geometric mean diameter.

We diagnosed that the CDF_N and CDF_V are 61% and 7% for D_{GA} = 2 um, 83% and 21% for D_{GA} = 3 um, and 93% and
38% for D_{GA} = 4 um. In other words, GA accounts for 39%, 17% and 7% coarse-mode aerosol number at 2, 3, and 4 um,
respectively.

We then calculated the fractions of column-integrated burden of coarse-mode interstitial aerosol number (num_a3) to the
column-integrated burden of total interstitial aerosol number (f_{a3}), the column-integrated burden of coarse-mode cloud-borne
aerosol number ($B_{\mathrm{num\_c3}}$) to the column-integrated burden of total cloud-borne aerosol number (f_{c3}), and the column-integrated

GCCN number burden to the column-integrated coarse-mode cloud-borne aerosol number burden (f_{GCCN}):

$$f_{a3} = \frac{[num\_a3]}{[num\_a1] + [num\_a2] + [num\_a3] + [num\_a4]}, \tag{7}$$

$$f_{c3} = \frac{[num\_c3]}{[num\_c1] + [num\_c2] + [num\_c3] + [num\_c4]}, \tag{8}$$

145    $$f_{GCCN} = \frac{[num\_GCCN]}{[num\_c3]}, \tag{9}$$

where the brackets [ ] denote column integral from surface to the top of the mode, num_a1, num_a2, num_a3, and num_a4 are the interstitial aerosol number mixing ratios in the accumulation, Aitken, coarse, and primary carbon modes. Similarly, num_c1, num_c2, num_c3, and num_c4 are the cloud-borne aerosol number mixing ratios in those four modes.

In Figure 2, we find that the coarse mode aerosol accounts for only 0.06% of interstitial aerosol particles globally. The ratio

150 can reach up to 0.1% over the sea salt source regions over the ocean and 1% for the dust source regions in North Africa, middle Asia and Australia. The ratio of cloud-borne coarse aerosol increased by a factor of 10 to 0.69%. This is because they have larger sizes and are more easily activated compared to other aerosol modes. If using the threshold of 2 μm defined for GCCN diameters, the number fraction of GCCN takes up 2.65% of num_c3. Combing the num_c3 ratio, we can see that GCCN occupies less than 0.02% of CCN. The global mean number burden of GCCN is 1.92×10^6 m^{-2} and it is close to the simulated

155 value by Posselt and Lohmann (2008). Higher concentrations of GCCN are found over the ocean storm track regions, which are characterized by strong winds and high sea-salt emissions. We anticipate GCCN effects to be most pronounced in these regions.
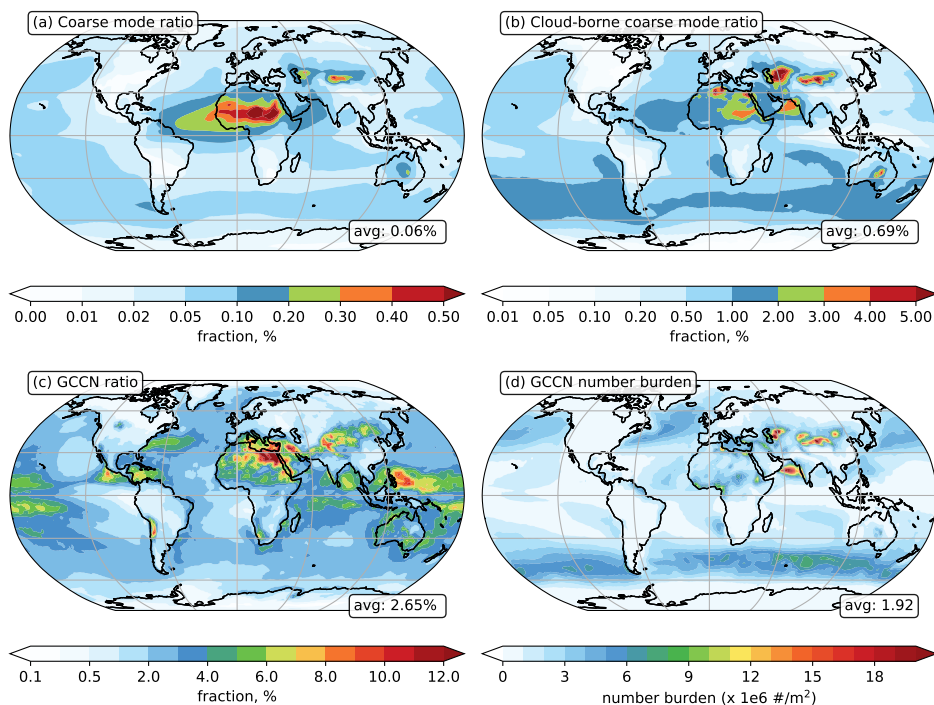
Figure 2. Spatial distribution of (a) coarse mode ratio, (b) cloud-borne coarse mode ratio, (c) GCCN ratio and (d) GCCN number burden. Values at the bottom right are for the global area weighted mean. The threshold used for GCCN in the figure is 2 um.

Interstitial and cloud-borne aerosol particles of different modes respond differently in inertially-limited and directly-activated cases (Fig. 3). As the vertical profiles show, comparing with the control cases, there are negligible changes for most interstitial
160 and cloud-borne modes in the inertially-limited cases GA_inert_D1 and GA_inert_D2. The slight increase in cloud-borne accumulation mode (num_c1) and Aitken mode (num_c2) is attributed to the removal of GA before activation, leading to more accessible water for these smaller particles. As for the directly-activated cases, all cloud-borne aerosols decrease due to less available liquid water after transferring GCCN to drizzle droplets. The decrease in interstitial accumulation (num_a1) and coarse (num_a3) mode, along with the increase of interstitial Aitken mode (num_a2), results from the balance between
165 enhanced activation due to the removal of GA before activation and the reduced activation due to limited available liquid water.
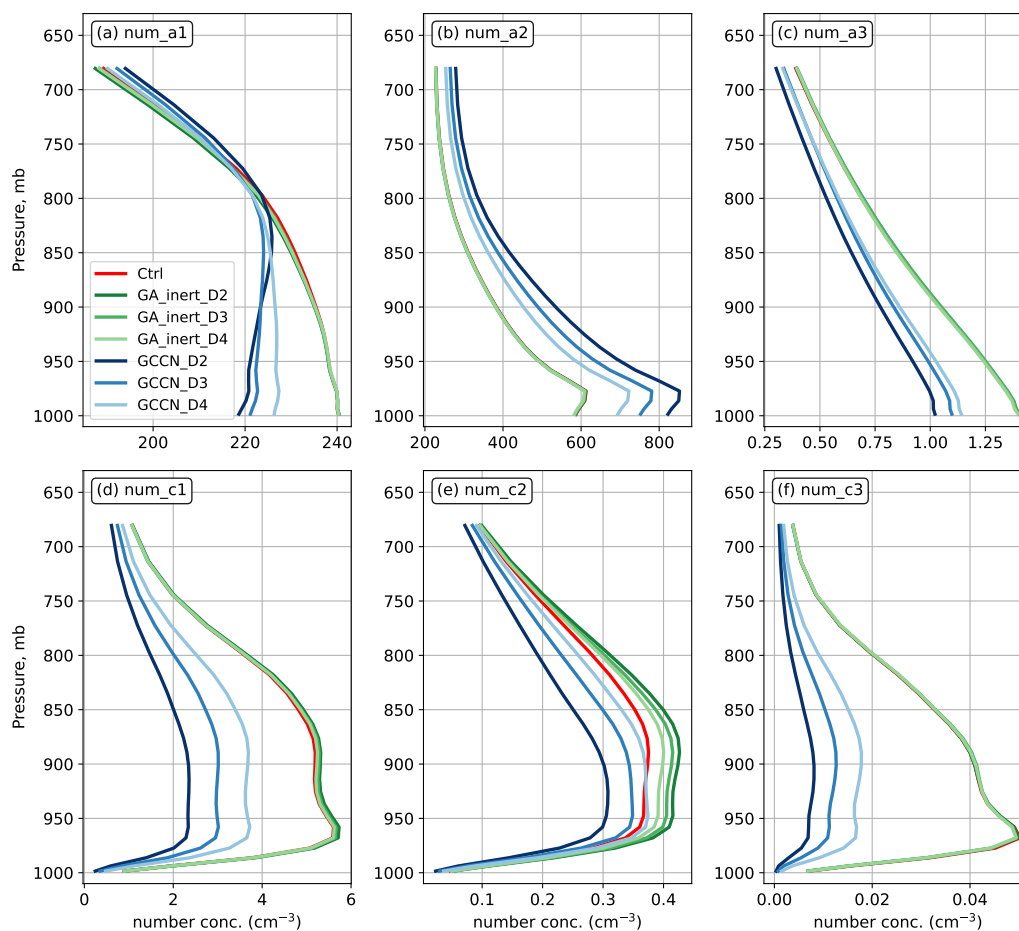
Figure 3. Global area-weighted average profiles of (a) interstitial accumulation mode number concentration (num_a1), (b) interstitial Aitken mode number concentration (num_a2), (c) interstitial coarse mode number concentration (num_a3), (d) cloud-borne accumulation mode number concentration (num_c1), (e) cloud-borne accumulation mode (num_c2) and (f) cloud-borne coarse mode (num_c3). Different colors are for different cases.

Since the cases in the same scheme displayed similar spatial patterns but with different amplitudes, for the following spatial distribution analysis, we chose GCCN_D4 in directly-activated scheme and GA_inert_D4 in inertially-limited scheme for comparisons. Figure 4 shows the spatial distribution of vertically-integrated cloud droplets number concentration (CDNC) of different cases. By directly activated to rain droplets, CDNC decreased more than 15% globally in GCCN_D4, and the changes are more substantial over mid-latitude ocean regions. As for GA_inert_D2, CDNC shows slight increase globally (0.58%) attributed to the cloud droplets formation from smaller particles.
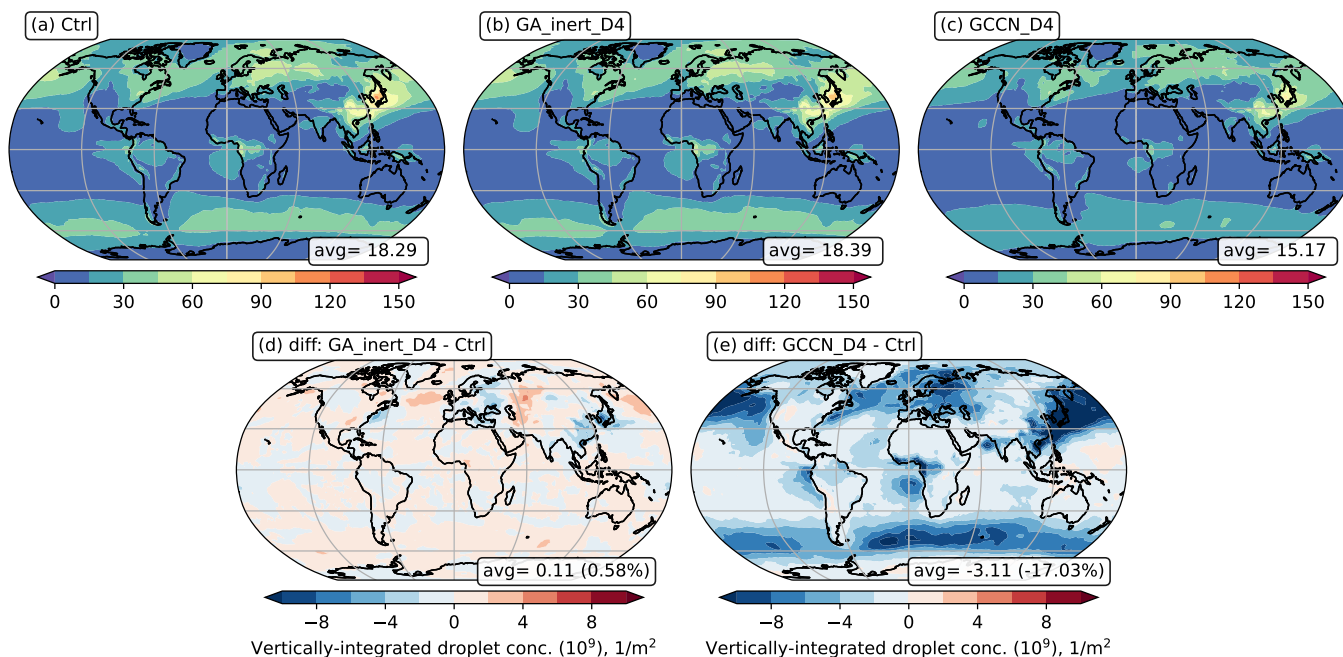
Figure 4. Spatial distribution of vertically-integrated droplet concentration in (a) Ctrl, (b) GA_inert_D4, and (c) GCCN_D4. (d) and (e) are for the differences between the cases. Values at the bottom right are for the global area weighted mean.

Figure 5 shows the total liquid water path (LWP) distribution. The displayed LWP includes both deep convective liquid clouds simulated by ZM scheme, and stratiform and shallow cumulus liquid clouds simulated by MG2 scheme. The patterns are similar among the cases, with abundant liquid water over the southern and northern ocean region with the value of over

175    $100 \, \mathrm{g \, m^{-2}}$. We can also see some liquid clouds over the tropics, where clouds can develop deeply and remain liquid. It is also prevalent off the west coast of Africa and South America continents due to large-scale subsidence (Quaas and Gryspeerdt, 2022). These simulated liquid water patterns are consistent with the satellite observations (Platnick et al., 2016).
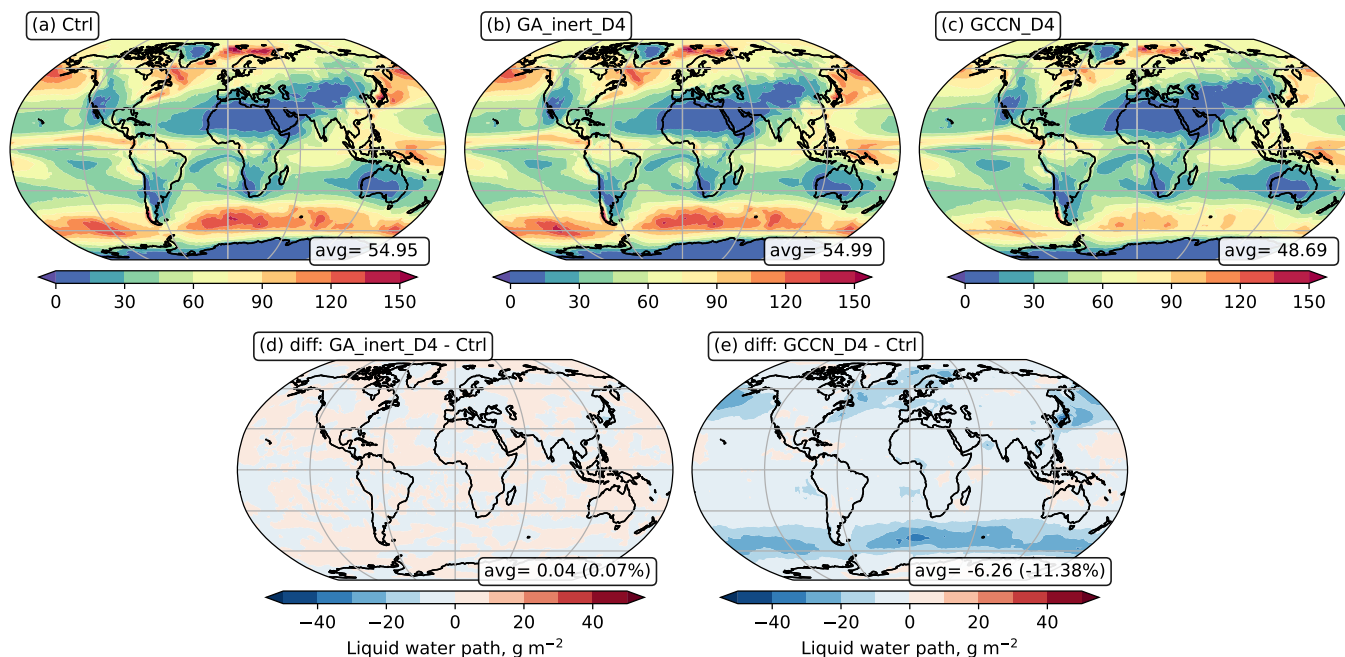
Figure 5. Same as Fig 4, but for liquid water path.

As for the differences between the cases, in the directly-activated simulations, the effects of GCCN on LWP are most obvious over the storm track ocean regions in both hemispheres (Figure 5e) where high wind occurs and more GCCN are emitted. In GCCN_D4 with assuming GCCN diameter of 4 μm, LWP decreases by 11.38%, from 54.95 to 48.69 $\mathrm{g\,m^{-2}}$. The differences are more significant if assuming smaller GCCN threshold. As shown in Table 2, LWP further decreases to 38.85 $\mathrm{g\,m^{-2}}$ in GCCN_D2. In inertially-limited case GA_inert_D4, the changes are subtle, with a global mean difference of less than 0.1%.

Table 2 also shows the LWP only from stratiform and shallow cumulus liquid clouds, and we can see the differences in LWP (ZM+MG2) can be explained by the changes in LWP (MG2). This makes sense given that we only considered the GCCN effects through the MG2 scheme. The rain water path (RWP) spatial pattern (Figure S1) shows GCCN leads to increased RWP over storm track regions GCCN_D4, but the amplitude is smaller than LWP. RWP increased from 12.18 $\mathrm{g\,m^{-2}}$ in Ctrl to 13.63 $\mathrm{g\,m^{-2}}$ in GCCN_D4. Similar to the changes in LWP, the RWP difference is also insignificant in GA_inert_D4 case, with global mean change less than 0.1%. Given the limited impact of the GA inertially-limited scheme on LWP and RWP, the subsequent analysis will focus on directly-activated experiments.
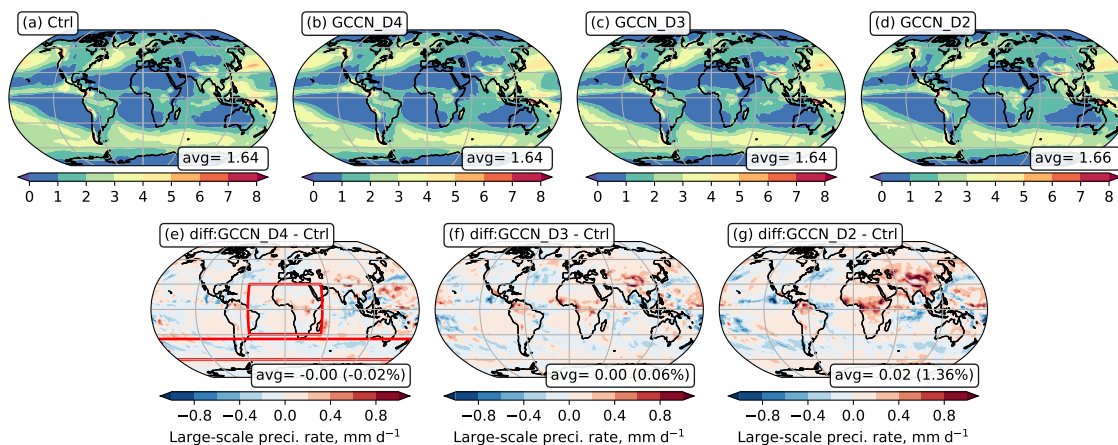
Figure 6. Spatial distribution of Large-scale precipitation rate in (a) Ctrl, (b) GCCN_D4, (c) GCCN_D3 and (d) GCCN_D2. (e), (f) and (g) are for the differences between the cases. Values at the bottom right are for the global area weighted mean. The regions in the red box are for evaluation in section 4.

Table 2. Global mean cloud and precipitation variables

Variables	Ctrl	GA_inert_D4	GA_inert_D3	GA_inert_D2	GCCN_D4	GCCN_D3	GCCN_D2
LWP (ZM+MG2)	54.95	54.99 (0.04)	54.99 (0.04)	55.04 (0.09)	48.69 (–6.26)	44.59 (– 10.36)	38.85 (–16.10)
LWP (MG2)	40.01	40.01 (0.0)	40.05 (0.04)	40.07 (0.06)	33.85 (–6.16)	29.82 (–10.19)	24.26 (–15.75)
RWP	12.18	12.17 (–0.01)	12.17 (–0.01)	12.10 (–0.08)	13.63 (1.45)	14.39 (2.21)	15.52 (2.39)
PRECL	1.64	1.64 (0.0)	1.64 (0.0)	1.64 (0.0)	1.64 (0.0)	1.64 (0.0)	1.66 (0.02)

*: ZM is for deep convection scheme, and MG2 is for stratiform and shallow cumulus scheme. Values in the brackets are for the differences between sensitivity cases and control casse. LWP and RWP are in the unit of $g\,m^{-2}$. PRECL is in the unit of $mm\,d^{-1}$.

190   Compared with the changes in LWP and RWP, GCCN impacts on surface precipitation rate are local and much smaller. As shown in Fig. 6, the global mean large-scale precipitation rate (PRECL) changes in all the GCCN cases are less than 2%, and the changes are close to zero in the inertially-limited cases (Tabel 2). The minor PRECL changes in the inertially-limited cases are reasonable considering the small perturbations in LWP and RWP. For the diretly-activated GCCN cases, we find the negilible surface rate change is due to the excessive rain water from GCCN are removed by evaporation, as illustrated in Fig 7.

195   The rain production rates in Fig. 7(a) are the sum of autoconversion, accretion and GCCN rain rates. The increase of the rain production rates in GCCN cases are due to the additional rain formation from GCCN. The accretion rates remain nearly unchanged in the cloud, while the autoconversion rates decrease as a result of decreased liquid water content (Figure S2). The rise in rain production rates aligns with the simulated RWP trend. The escalation in evaporation rates offset the rise in rain

production rates. The evaporation rates of falling precipitation are over 2.8×10^{-15} kg kg^{-1} s^{-1} in the GCCN cases, while it

200 is less than 2×10^{-15} kg kg^{-1} s^{-1} in control case.
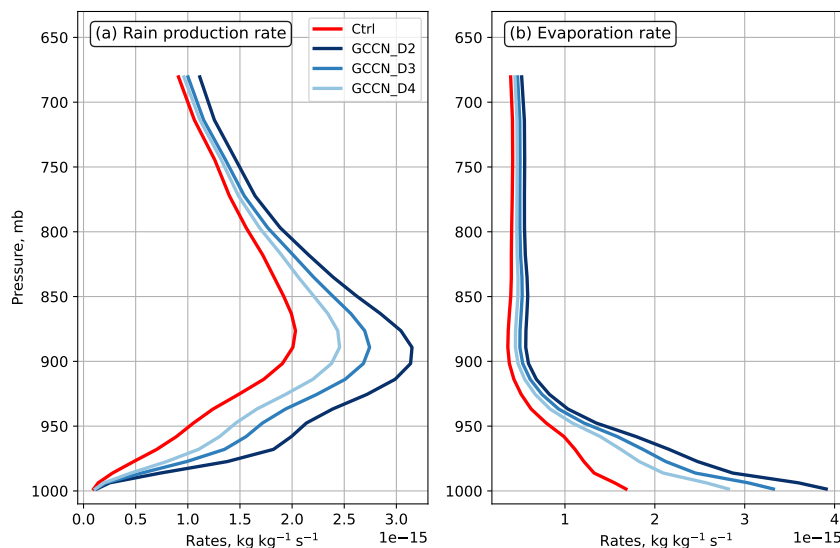
Figure 7. Gobal area-weighted average profiles of (a) rain production rate and (b)evaporation rate. Different colors are for different cases.

4 GCCN effects on precipitation susceptibility to aerosol

Previous studies have reported that E3SM produces strong ERFaci (Rasch et al., 2019; Ma et al., 2022; Zhang et al., 2022; Golaz et al., 2019, 2022) compared to best estimates (Bellouin et al., 2020). Many studies have found that the precipitation suppression is overly strong in climate models, which points to deficiencies in the precipitation process representation (e.g.,

205 Wang et al. (2012)). More recently, Varble et al. (2023) showed that the cloud albedo susceptibility in E3SM is overly strong compared to observations, and the negative LWP adjustment in the model fails to mute the Twomey effect. Because the GCCN mechanism acts as a warm rain process, in addition to autoconversion and accretion, the precipitation susceptibility to aerosol might change.

In a recent study by Liu et al. (2022), the authors found that coarse sea spray aerosol exerts comparable reverse effects on

210 surface precipitation fluxes as fine aerosol particles by analyzing observational and reanalysis data. To maintain consistency with the data selection criteria employed by Liu et al. (2022), we used the hourly output data from nudging simulations and selected oceanic liquid clouds with cloud top temperature greater than 265 K in the tropical region between 50° W to 50° E and 30° S to 30° N. We also selected the mid-latitude southern ocean region (30° S to 60° S) where the GCCN effects are most substantial, as the regions outlined in Figure 6. Fine mode mass is the sum of all the species in Aitken mode, accumulation

215 mode and primary carbon mode, and coarse mode mass is the sum of coarse mode species. We only considered the species masses at surface level. Rain flux is the large-scale precipitation rate and the in-cloud liquid water path is for liquid clouds.
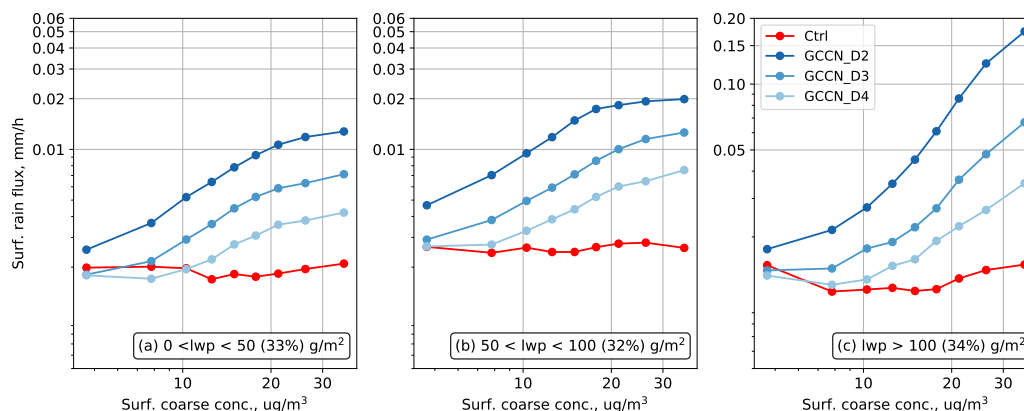
Figure 8. Correlation between surface coarse mode concentration and surface rain fluxes at three different LWP levels over tropical ocean regions: (a) $0 < \text{LWP} < 50 \, \text{g m}^{-2}$, (b) $50 < \text{LWP} < 100 \, \text{g m}^{-2}$, and (c) $\text{LWP} > 100 \, \text{g m}^{-2}$. Different colors represent different cases and the dots represent the mean value in each tenth quantile bin of surface coarse mode concentration. Percentage in the legend are for the sample ratio in the corresponding LWP ranges.

Figure 8 shows the correlation between surface coarse concentration and surface rain fluxes at three different LWP levels. In the Ctrl case, there is no clear tendency between surface rain fluxes and coarse mode concentration at different LWP ranges. After incorporating GCCN, the model produces a positive correlation between surface rain flux and coarse aerosol mass mixing ratio, which is consistent with the observations in Liu et al. (2022). This positive correlation becomes more pronounced at high LWP environment.

In order to disentangle the fine mode and coarse mode impacts on surface rain fluxes, we further analyzed the correlation at fixed fine mode concentration (Figure 9). We find that the positive correlation appears at the low fine mode condition ($0 < N_{\text{fine}}$ <= 25%). As fine mode aerosol increases, we find that the model produces a precipitation suppression effect when the coarse mode aerosol concentration is low. Incorporating GCCN results in precipitation enhancement at higher coarse mode aerosol concentration. Our results show that the directly-activated GCCN mechanism produces simulations that are consistent with the LES results Dziekan et al. (2021). At higher fine mode conditions ($N_{\text{fine}} > 50\%$), the average increasing factor of surface rain fluxes from lowest to highest coarse mode bin in GCCN cases is between 2 and 4, which is also close to the amplitude of the observed value in Liu et al. (2022). These results demonstrate that the directly-activated GCCN mehcanism is important in simulating the response of surface rain flux to coarse mode aerosol concentration, and, hence, reducing the precipitation susceptibility to aerosol.

As for the southern ocean regions, we can find the surface rain correlation with surface coarse mode concentration in fixed LWP (Figure S3) and fixed fine mode (Figure S4) are similar between the control and GCCN cases, with all the cases displaying clear positive correlation between rain rates and coarse mode concentration. The different behaviour of GCCN impacts in southern ocean and tropical ocean regions can be primarily attributed to the variations in precipitation rates in these areas. The simulated large-scale precipitation rates in southern ocean is $0.09 \, \text{mm h}^{-1}$, while the mean rate is only $0.01 \, \text{mm h}^{-1}$. The

GCCN effects are significant in regions with low precipitation rates, whereas the effects are inhibited in regions with greater precipitation rates.
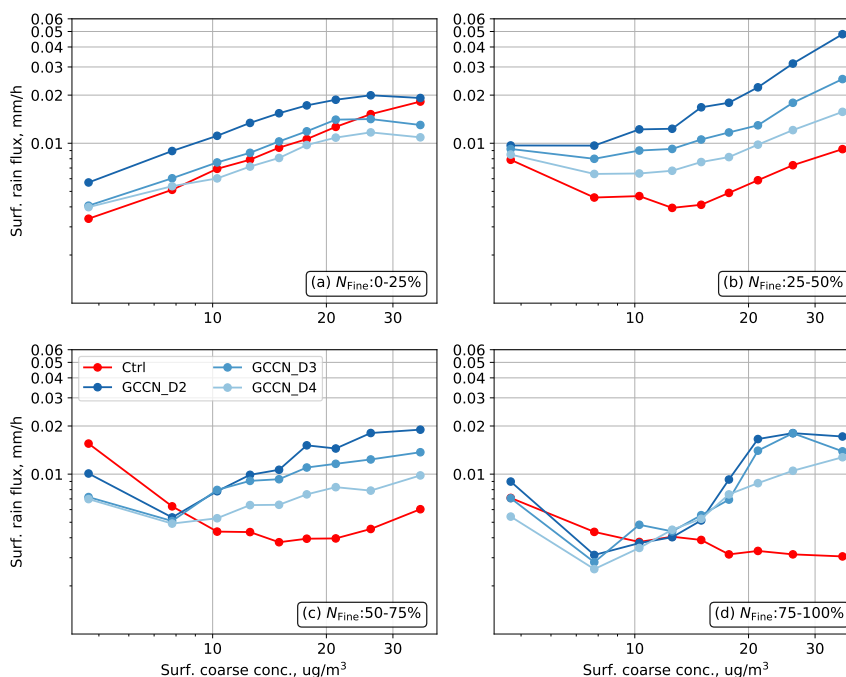
Figure 9. Correlation between surface coarse mode concentration and surface rain fluxes at four different fine mode surface concentration quantiles over tropical ocean regions: (a) $0 < N_{\text{fine}} <= 25\%$, (b) $25 < N_{\text{fine}} <= 25\%$, (c) $50 < N_{\text{fine}} < 75\%$ and (d) $75 < N_{\text{fine}} < 100\%$. Same as Fig. 8, colors are for different cases and the dots represent the mean value in each tenth quantile bin of surface coarse mode concentration.

5   GCCN effects on radiative forcing

240   In this section, we will discuss the two GA scheme impacts on radiative forcing. Figure 10 shows the spatial distribution of shortwave cloud radiative effect (SWCRE). SWCRE decreases almost everywhere after considering GCCN, with global mean SWCRE reduces from –47.54 in Ctrl to –44.79 W m^{-2} in GCCN_D4. The signals are more obvious over ocean storm tracks and off the west coasts of Peru and Chile, where the SWCRE is reduced by more than 6 W m^{-2}. These changes are associated with the reduced low-level liquid cloud water introduced by GCCN. The changes introduced by inertially-limited mechanism

245   are much smaller with global mean change less than 1%.
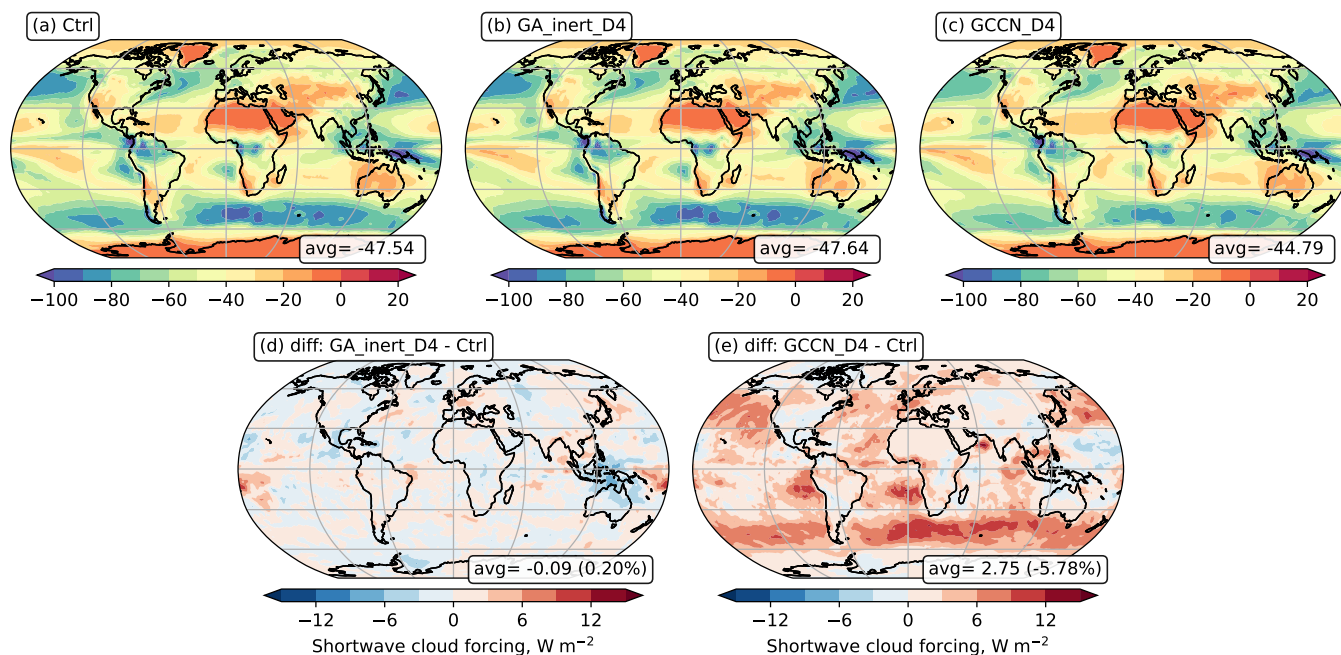
Figure 10. Same as figure 4, but for shortwave cloud radiative effect.

The comparison of SWCRE zonal variation between model simulations and measurements is illustrated in Fig. 11. The measurements are from Clouds and the Earth's Radiant Energy System Energy Balanced and Filled datasets (CERES_EBAF, Loeb et al. (2018)). The SWCRE peaks and troughs in the observations are well represented by all simulations, and are most within the 0.5σ ranges. For the cases considering GCCN directly-activated effects, SWCRE substantially decreases over southern storm track regions, while the change is negligible over the tropics. These changes are associated with the modifications in LWP. The resulting decreasing SWCRE zonal variations introduced by GCCN could have important implications for Earth's energy balance and large-scale dynamics (Soden and Chung, 2017). It's worth noting that in the GCCN_D2 cases, when assuming GCCN size with 2 μm, there was a significant decrease in liquid water content and a less pronounced negative forcing simulated over the mid-latitude oceans.
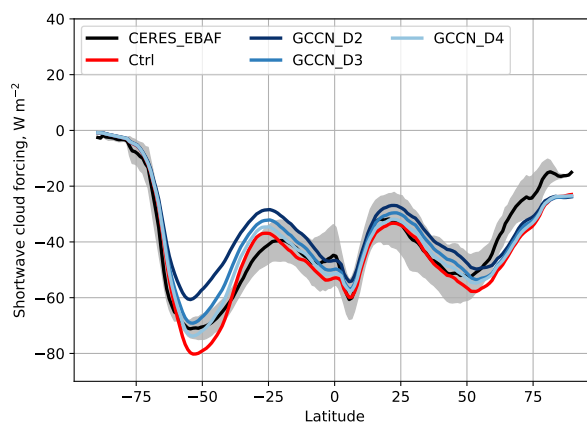
Figure 11. Zonal average of shortwave radiative effect from CERES_EBAF and model simulations. Black is for CERES_EBAF observation and red is for Ctrl. Blue colors are for the three directly-activated cases. Shade area is for 0.5σ of the observations.

As discussed in Golaz et al. (2022), E3SMv2 produces a slightly weaker aerosol ERF of –1.52 W/m² than E3SMv1's –1.65 W/m². In this study, because GCCN reduces the precipitation susceptibility to aerosol, their impacts on aerosol ERF could be substantial. Following the radiative forcing decomposition method developed by Ghan (2013), we calculated the total aerosol radiative forcing $\mathrm{ERF_{tot}}$, aerosol-cloud radiative forcing $\mathrm{ERF_{aci}}$, aerosol direct radiative forcing $\mathrm{ERF_{ari}}$ and surface albedo forcing $\mathrm{ERF_{surf}}$ using:

$$\mathrm{ERF_{ari}} = \Delta(F - F_{\mathrm{clean}}), \tag{10}$$

$$\mathrm{ERF_{aci}} = \Delta(F_{\mathrm{clean}} - F_{\mathrm{clear,clean}}), \tag{11}$$

$$\mathrm{ERF_{surf}} = \Delta(F_{\mathrm{clear,clean}}), \tag{12}$$

$$\mathrm{ERF_{tot}} = \mathrm{ERF_{ari}} + \mathrm{ERF_{aci}} + \mathrm{ERF_{surf}}, \tag{13}$$

where F is the all-sky top of model radiative flux, F_{clean} is the radiative flux without aerosol, and $F_{\mathrm{clear,clean}}$ is the radiative flux without aerosol and cloud.

As summarized in Table 3, the radiative forcing in inertially-limited cases are very similar to the control case, while directly-activated GCCN mechanism affects $\mathrm{ERF_{aer}}$ significantly. The impact is significantly larger when smaller GCCN size thresholds are used. The global mean $\mathrm{ERF_{tot}}$ decreased from –1.29 W/m² in Ctrl to –0.84 W/m² in GCCN_D2. This decrease is mostly attributed to the decrease in ERFaci, which decreases from –1.37 W/m² in Ctrl to –0.94 W/m² in GCCN_D2. Furthermore, it is worth noting that E3SM produces a positive ERFari because of overly strong aerosol absorption. Incorporating GCCN also reduces this bias by enhancing wet scavenging of absorbing aerosol (e.g., black carbon) in mid-latitudes, bring the model in better agreement with IPCC AR6 estimates (Forster et al., 2021).

Table 3. Radiative forcing values (W/m^2) in different cases

Variables	Ctrl	GA_inert_D4	GA_inert_D3	GA_inert_D2	GCCN_D4	GCCN_D3	GCCN_D2	Reference
SWCRE	–47.54	–47.64	–47.61	–47.71	–44.79	–42.53	–38.79	–45.31
ERF_{aer}	–1.29	–1.21	–1.07	–1.24	–1.20	–0.95	–0.84	–1.1 [–1.7, –0.4]
ERF_{aci}	–1.37	–1.38	–1.30	–1.39	–1.23	–1.07	–0.94	–0.84 [–1.45, –0.25]
ERF_{ari}	0.08	0.09	0.09	0.09	0.05	0.01	-0.02	–0.22 [–0.47, 0.04]

*: SWCRE reference is from CERES_EBAF (Loeb et al., 2018) and ERF component references are from IPCC
AR6 (Forster et al., 2021).

6 Summary and conclusion

In this study, we developed a parameterization to represent the giant aerosol effects in an Earth system model. For the inertially-
275 limited mechanism, coarse particles with diameters larger than 2, 3 or 4 µm are treated as GA and removed before activation.
For the directly-activated mechanism, we remove GA and further determine the abundance of GCCN from cloud-borne coarse
aerosol with diameter larger than the same threshold used in the inertially-limited case, and short-circuit these giant aerosol to
form rain droplets with the size of 25 µm. We performed global climatology and nudged simulations to assess their impacts on
cloud and rain properties, as well as radiative forcing.

280   For the three threshold sizes used for GA —2, 3 or 4 µm—coarse mode number concentration are reduced by 39%, 17%,
and 7% respectively before activation, respectively, which result in more smaller activated particles and increasing cloud
droplets number concentration. However, if only considering the inertially-limited effects, these changes do not result in much
differences in simulated LWP and RWP, and radiative forcing, as we find in the GA_inert_D2, GA_inert_D3, and GA_inert_D4
cases.

285   In the directly-activated experiments, accounting for both GA kinetic effect and condensational growth, transferring less than
0.02% of CCN (the ratio of GCCN) to rain droplets results in substantial changes in LWP and RWP. With assuming activated
rain droplets size 25 µm formed on these GCCN particles, LWP decrease –11.38% globally and RWP increased 11.91%
in GCCN_D4, and the effects are most significant over storm track regions in southern and northern ocean. If smaller GCCN
thresholds (2 and 3 µm) are used, the effects are more pronounced, potentially leading to unrealistic decreases in LWP. The
290 LWP and RWP changes only translated to smaller changes in surface precipitation rates at global scale. This can be explained
by the increasing rates of evaporation of falling precipitation in lower levels in the GCCN cases. Furthermore, we find that
including GCCN enables the model to reproduce the positive correlation between between surface coarse mode concentration
and surface rain fluxes observed by Liu et al. (2022). This feature essentially reduces the precipitation susceptibility to aerosol,
which leads to weaker aerosol ERF, bringing in the model in better agreement with state-of-the-art estimates reported in IPCC
295 AR6 (Forster et al., 2021). These results demonstrate that GCCN has a significant impact on the simulated climate.

It should be noted that we maximized the inertially-limited effects by removing these larger particle before activation. In theory, these GA particles should still absorb water vapor, even though they do not reach their critical sizes to be activated as described by the Köhler equilibrium theory. With this treatment, we still find the overall effects to be negligible. It is possible that this effect is small. Another possibility is that the giant aerosol in the model is only a small fraction of total aerosol, so that their effects are muted. As discussed by Adebiyi and Kok (2020) and Hartery et al. (2020), there are still uncertainties in representing the emissions for coarse mode sea salt and dust particles in climate models. Future studies on the inertially-limited effects with improved giant aerosol simulations is highly desired.

Code and data availability. The default E3SMv2 codes can be found at E3SM Project (2022). The codes with new giant aerosol parameter-ization are available at Yao and Ma (2024b). The simulation output climatology used for analysis is available at Yao and Ma (2024c). The nudged simulation hourly output for susceptibility analysis can be accessed at Yao and Ma (2024a, d).

Author contributions. Y. Yao and P. Ma initiated the model framework for this work. Y. Yao and P. Ma performed the analysis and prepared the manuscript, with edits from co-authors. Y. Yao, P. Ma, Y. Qin, H. Wan, K. Zhang and B. Singh revised the codes in E3SM to include giant aerosol effects. M. Christensen provided the observation data for evaluation. M. Huang and Y. Qin help write the plotting codes. M. Ovchinnikov aided in interpreting the results. All the co-authors provided insightful comments for the manuscript.

Competing interests. One of the (co-) authors is a member of the editorial board of Geoscientific Model Development.

Acknowledgements. The study was supported as part of the Enabling Aerosol–cloud interactions at GLobal convection-permitting scalES (EAGLES) project (project no. 74358) sponsored by the United States Department of Energy (DOE), Office of Science, Office of Bio-logical and Environmental Research (BER), Earth System Model Development (ESMD) program area. The Pacific Northwest National Laboratory (PNNL) is operated for the DOE by the Battelle Memorial Institute under Contract DE-AC05-76RL01830. The research used high-performance computing resources from the PNNL Research Computing, the BER Earth System Modeling program's Compy computing cluster located at PNNL, and resources of the National Energy Research Scientific Computing Center (NERSC), a U.S. Department of Energy Office of Science User Facility located at Lawrence Berkeley National Laboratory, operated under Contract No. DE-AC02-05CH11231, using NERSC awards ALCC-ERCAP0025938 and BER-ERCAP0024471.

References

Abdul-Razzak, H. and Ghan, S. J.: A parameterization of aerosol activation: 2. Multiple aerosol types, Journal of Geophysical Research: Atmospheres, 105, 6837–6844, 2000.

Adebiyi, A. A. and Kok, J. F.: Climate models miss most of the coarse dust in the atmosphere, Science advances, 6, eaaz9507, 2020.

Albrecht, B. A.: Aerosols, cloud microphysics, and fractional cloudiness, Science, 245, 1227–1230, 1989.

Barahona, D., West, R., Stier, P., Romakkaniemi, S., Kokkola, H., and Nenes, A.: Comprehensively accounting for the effect of giant CCN in cloud activation parameterizations, Atmospheric Chemistry and Physics, 10, 2467–2473, 2010.

Bellouin, N., Quaas, J., Gryspeerdt, E., Kinne, S., Stier, P., Watson-Parris, D., Boucher, O., Carslaw, K. S., Christensen, M., Daniau, A.-L., et al.: Bounding global aerosol radiative forcing of climate change, Reviews of Geophysics, 58, e2019RG000 660, 2020.

Blyth, A. M., Lowenstein, J. H., Huang, Y., Cui, Z., Davies, S., and Carslaw, K. S.: The production of warm rain in shallow maritime cumulus clouds, Quarterly Journal of the Royal Meteorological Society, 139, 20–31, 2013.

Cheng, W. Y., Carrió, G. G., Cotton, W. R., and Saleeby, S. M.: Influence of cloud condensation and giant cloud condensation nuclei on the development of precipitating trade wind cumuli in a large eddy simulation, Journal of Geophysical Research: Atmospheres, 114, 2009.

Dusek, U., Frank, G., Hildebrandt, L., Curtius, J., Schneider, J., Walter, S., Chand, D., Drewnick, F., Hings, S., Jung, D., et al.: Size matters more than chemistry for cloud-nucleating ability of aerosol particles, Science, 312, 1375–1378, 2006.

Dziekan, P., Jensen, J. B., Grabowski, W. W., and Pawlowska, H.: Impact of giant sea salt aerosol particles on precipitation in marine cumuli and stratocumuli: Lagrangian Cloud Model simulations, Journal of the Atmospheric Sciences, 78, 4127–4142, 2021.

E3SM Project, D.: Energy Exascale Earth System Model v2.0.2, [Computer Software] https://doi.org/10.11578/E3SM/dc.20221118.3, https://doi.org/10.11578/E3SM/dc.20221118.3, 2022.

Feingold, G., Cotton, W. R., Kreidenweis, S. M., and Davis, J. T.: The impact of giant cloud condensation nuclei on drizzle formation in stratocumulus: Implications for cloud radiative properties, Journal of the atmospheric sciences, 56, 4100–4117, 1999.

Feng, Y., Wang, H., Rasch, P., Zhang, K., Lin, W., Tang, Q., Xie, S., Hamilton, D., Mahowald, N., and Yu, H.: Global dust cycle and direct radiative effect in E3SM version 1: Impact of increasing model resolution, Journal of Advances in Modeling Earth Systems, 14, e2021MS002 909, 2022.

Forster, P., Storelvmo, T., Armour, K., Collins, W., Dufresne, J.-L., Frame, D., Lunt, D., Mauritsen, T., Palmer, M., Watanabe, M., Wild, M., and Zhang, H.: The Earth's Energy Budget, Climate Feedbacks, and Climate Sensitivity, p. 923–1054, Cambridge University Press, Cambridge, United Kingdom and New York, NY, USA, https://doi.org/10.1017/9781009157896.009, 2021.

Froyd, K. D., Yu, P., Schill, G. P., Brock, C. A., Kupc, A., Williamson, C. J., Jensen, E. J., Ray, E., Rosenlof, K. H., Bian, H., et al.: Dominant role of mineral dust in cirrus cloud formation revealed by global-scale measurements, Nature Geoscience, 15, 177–183, 2022.

Gettelman, A. and Morrison, H.: Advanced two-moment bulk microphysics for global models. Part I: Off-line tests and comparison with other schemes, Journal of Climate, 28, 1268–1287, 2015.

Ghan, S. J.: Estimating aerosol effects on cloud radiative forcing, Atmospheric Chemistry and Physics, 13, 9971–9974, 2013.

Golaz, J.-C., Larson, V. E., and Cotton, W. R.: A PDF-based model for boundary layer clouds. Part I: Method and model description, Journal of the atmospheric sciences, 59, 3540–3551, 2002.

Golaz, J.-C., Caldwell, P. M., Van Roekel, L. P., Petersen, M. R., Tang, Q., Wolfe, J. D., Abeshu, G., Anantharaj, V., Asay-Davis, X. S., Bader, D. C., et al.: The DOE E3SM coupled model version 1: Overview and evaluation at standard resolution, Journal of Advances in Modeling Earth Systems, 11, 2089–2129, 2019.

Golaz, J.-C., Van Roekel, L. P., Zheng, X., Roberts, A. F., Wolfe, J. D., Lin, W., Bradley, A. M., Tang, Q., Maltrud, M. E., Forsyth, R. M., et al.: The DOE E3SM Model Version 2: overview of the physical model and initial model evaluation, Journal of Advances in Modeling Earth Systems, 14, 2022.

360   Gonzalez, M. E., Corral, A. F., Crosbie, E., Dadashazar, H., Diskin, G. S., Edwards, E.-L., Kirschler, S., Moore, R. H., Robinson, C. E., Schlosser, J. S., et al.: Relationships between supermicrometer particle concentrations and cloud water sea salt and dust concentrations: analysis of MONARC and ACTIVATE data, Environmental Science: Atmospheres, 2, 738–752, 2022.

Grosvenor, D. P., Field, P. R., Hill, A. A., and Shipway, B. J.: The relative importance of macrophysical and cloud albedo changes for aerosol-induced radiative effects in closed-cell stratocumulus: insight from the modelling of a case study, Atmospheric Chemistry and Physics,

365   17, 5155–5183, 2017.

Gryspeerdt, E., Stier, P., and Partridge, D.: Satellite observations of cloud regime development: the role of aerosol processes, Atmospheric Chemistry and Physics, 14, 1141–1158, 2014.

Gryspeerdt, E., Goren, T., Sourdeval, O., Quaas, J., Mülmenstädt, J., Dipu, S., Unglaub, C., Gettelman, A., and Christensen, M.: Constraining the aerosol influence on cloud liquid water path, Atmospheric Chemistry and Physics, 19, 5331–5347, 2019.

370   Hannah, W. M., Bradley, A. M., Guba, O., Tang, Q., Golaz, J.-C., and Wolfe, J.: Separating physics and dynamics grids for improved computational efficiency in spectral element earth system models, Journal of Advances in Modeling Earth Systems, 13, e2020MS002 419, 2021.

Hartery, S., Toohey, D., Revell, L., Sellegri, K., Kuma, P., Harvey, M., and McDonald, A. J.: Constraining the surface flux of sea spray particles from the Southern Ocean, Journal of Geophysical Research: Atmospheres, 125, e2019JD032 026, 2020.

375   Jensen, J. B. and Lee, S.: Giant sea-salt aerosols and warm rain formation in marine stratocumulus, Journal of the atmospheric sciences, 65, 3678–3694, 2008.

Jensen, J. B. and Nugent, A. D.: Condensational growth of drops formed on giant sea-salt aerosol particles, Journal of the atmospheric sciences, 74, 679–697, 2017.

Lasher-Trapp, S. G., Knight, C. A., and Straka, J. M.: Early radar echoes from ultragiant aerosol in a cumulus congestus: Modeling and

380   observations, Journal of the atmospheric sciences, 58, 3545–3562, 2001.

Liu, F., Mao, F., Rosenfeld, D., Pan, Z., Zang, L., Zhu, Y., Yin, J., and Gong, W.: Opposing comparable large effects of fine aerosols and coarse sea spray on marine warm clouds, Communications Earth & Environment, 3, 232, 2022.

Liu, X., Easter, R. C., Ghan, S. J., Zaveri, R., Rasch, P., Shi, X., Lamarque, J.-F., Gettelman, A., Morrison, H., Vitt, F., et al.: Toward a minimal representation of aerosols in climate models: Description and evaluation in the Community Atmosphere Model CAM5, Geoscientific

385   Model Development, 5, 709–739, 2012.

Liu, X., Ma, P.-L., Wang, H., Tilmes, S., Singh, B., Easter, R., Ghan, S., and Rasch, P.: Description and evaluation of a new four-mode version of the Modal Aerosol Module (MAM4) within version 5.3 of the Community Atmosphere Model, Geoscientific Model Development, 9, 505–522, 2016.

Loeb, N. G., Doelling, D. R., Wang, H., Su, W., Nguyen, C., Corbett, J. G., Liang, L., Mitrescu, C., Rose, F. G., and Kato, S.: Clouds and the

390   earth's radiant energy system (CERES) energy balanced and filled (EBAF) top-of-atmosphere (TOA) edition-4.0 data product, Journal of Climate, 31, 895–918, 2018.

Lohmann, U. and Feichter, J.: Global indirect aerosol effects: a review, Atmospheric Chemistry and Physics, 5, 715–737, 2005.

Ma, P.-L., Harrop, B. E., Larson, V. E., Neale, R. B., Gettelman, A., Morrison, H., Wang, H., Zhang, K., Klein, S. A., Zelinka, M. D., et al.: Better calibration of cloud parameterizations and subgrid effects increases the fidelity of the E3SM Atmosphere Model version 1, Geoscientific Model Development, 15, 2881–2916, 2022.

Mechem, D. B. and Kogan, Y. L.: A bulk parameterization of giant CCN, Journal of the atmospheric sciences, 65, 2458–2466, 2008.

Morales Betancourt, R. and Nenes, A.: Droplet activation parameterization: The population-splitting concept revisited, Geoscientific Model Development, 7, 2345–2357, 2014.

Nenes, A. and Seinfeld, J. H.: Parameterization of cloud droplet formation in global climate models, Journal of Geophysical Research: Atmospheres, 108, 2003.

Nenes, A., Ghan, S., Abdul-Razzak, H., Chuang, P. Y., and Seinfeld, J. H.: Kinetic limitations on cloud droplet formation and impact on cloud albedo, Tellus B: Chemical and Physical Meteorology, 53, 133–149, 2001.

Petters, M. and Kreidenweis, S.: A single parameter representation of hygroscopic growth and cloud condensation nucleus activity, Atmospheric Chemistry and Physics, 7, 1961–1971, 2007.

Platnick, S., Meyer, K. G., King, M. D., Wind, G., Amarasinghe, N., Marchant, B., Arnold, G. T., Zhang, Z., Hubanks, P. A., Holz, R. E., et al.: The MODIS cloud optical and microphysical products: Collection 6 updates and examples from Terra and Aqua, IEEE Transactions on Geoscience and Remote Sensing, 55, 502–525, 2016.

Posselt, R. and Lohmann, U.: Influence of Giant CCN on warm rain processes in the ECHAM5 GCM, Atmospheric Chemistry and Physics, 8, 3769–3788, 2008.

Quaas, J. and Gryspeerdt, E.: Chapter 12 - Aerosol-cloud interactions in liquid clouds, in: Aerosols and Climate, edited by Carslaw, K. S., pp. 489–544, Elsevier, https://doi.org/https://doi.org/10.1016/B978-0-12-819766-0.00019-5, 2022.

Rasch, P., Xie, S., Ma, P.-L., Lin, W., Wang, H., Tang, Q., Burrows, S., Caldwell, P., Zhang, K., Easter, R., et al.: An overview of the atmospheric component of the Energy Exascale Earth System Model, Journal of Advances in Modeling Earth Systems, 11, 2377–2411, 2019.

Riemer, N., Ault, A., West, M., Craig, R., and Curtis, J.: Aerosol mixing state: Measurements, modeling, and impacts, Reviews of Geophysics, 57, 187–249, 2019.

Soden, B. and Chung, E.-S.: The large-scale dynamical response of clouds to aerosol forcing, Journal of Climate, 30, 8783–8794, 2017.

Sun, J., Zhang, K., Wan, H., Ma, P.-L., Tang, Q., and Zhang, S.: Impact of nudging strategy on the climate representativeness and hindcast skill of constrained EAMv1 simulations, Journal of Advances in Modeling Earth Systems, 11, 3911–3933, 2019.

Twomey, S.: The influence of pollution on the shortwave albedo of clouds, Journal of the atmospheric sciences, 34, 1149–1152, 1977.

Varble, A. C., Ma, P.-L., Christensen, M. W., Mülmenstädt, J., Tang, S., and Fast, J.: Evaluation of liquid cloud albedo susceptibility in E3SM using coupled eastern North Atlantic surface and satellite retrievals, Atmospheric Chemistry and Physics, 23, 13 523–13 553, https://doi.org/10.5194/acp-23-13523-2023, 2023.

Vogl, C. J., Wan, H., Woodward, C. S., and Bui, Q. M.: Numerical coupling of aerosol emissions, dry removal, and turbulent mixing in the E3SM Atmosphere Model version 1 (EAMv1), part II: a semi-discrete error analysis framework for assessing coupling schemes, Geophysical Model Development, (in review), https://doi.org/10.48550/arXiv.2306.04929, 2023.

Wan, H., Zhang, K., Vogl, C. J., Woodward, C. S., Easter, R. C., Rasch, P. J., Feng, Y., and Wang, H.: Numerical coupling of aerosol emissions, dry removal, and turbulent mixing in the E3SM Atmosphere Model version 1 (EAMv1), part I: dust budget analyses and the impacts of a revised coupling scheme, Geophysical Model Development, (in review), https://doi.org/10.48550/arXiv.2306.05377, 2023.

430   Wang, H., Easter, R. C., Zhang, R., Ma, P.-L., Singh, B., Zhang, K., Ganguly, D., Rasch, P. J., Burrows, S. M., Ghan, S. J., et al.: Aerosols in the E3SM Version 1: New developments and their impacts on radiative forcing, Journal of Advances in Modeling Earth Systems, 12, e2019MS001 851, 2020.

Wang, M., Ghan, S., Liu, X., L'Ecuyer, T. S., Zhang, K., Morrison, H., Ovchinnikov, M., Easter, R., Marchand, R., Chand, D., et al.: Constraining cloud lifetime effects of aerosols using A-Train satellite observations, Geophysical Research Letters, 39, 2012.

435   Xie, S., Wang, Y.-C., Lin, W., Ma, H.-Y., Tang, Q., Tang, S., Zheng, X., Golaz, J.-C., Zhang, G. J., and Zhang, M.: Improved diurnal cycle of precipitation in E3SM with a revised convective triggering function, Journal of Advances in Modeling Earth Systems, 11, 2290–2310, 2019.

Yao, Y. and Ma, P.-L.: E3SMv2 hourly outputs Part I for paper: Representing the effects of giant aerosol in droplet nucleation in E3SMv2, https://doi.org/10.5281/zenodo.10672097, 2024a.

440   Yao, Y. and Ma, P.-L.: E3SMv2 codes with giant aerosol parameterization for paper: Representing the effects of giant aerosol in droplet nucleation in E3SMv2, https://doi.org/10.5281/zenodo.10672151, 2024b.

Yao, Y. and Ma, P.-L.: E3SMv2 climatology outputs for paper: Representing the effects of giant aerosol in droplet nucleation in E3SMv2, https://doi.org/10.5281/zenodo.10672153, 2024c.

Yao, Y. and Ma, P.-L.: E3SMv2 hourly outputs Part II for paper: Representing the effects of giant aerosol in droplet nucleation in E3SMv2,
445   https://doi.org/10.5281/zenodo.10685607, 2024d.

Yin, Y., Levin, Z., Reisin, T. G., and Tzivion, S.: The effects of giant cloud condensation nuclei on the development of precipitation in convective clouds—A numerical study, Atmospheric research, 53, 91–116, 2000.

Yu, F. and Luo, G.: Simulation of particle size distribution with a global aerosol model: contribution of nucleation to aerosol and CCN number concentrations, Atmospheric Chemistry and Physics, 9, 7691–7710, 2009.

450   Zhang, G. J. and McFarlane, N. A.: Sensitivity of climate simulations to the parameterization of cumulus convection in the Canadian Climate Centre general circulation model, Atmosphere-ocean, 33, 407–446, 1995.

Zhang, K., Zhang, W., Wan, H., Rasch, P. J., Ghan, S. J., Easter, R. C., Shi, X., Wang, Y., Wang, H., Ma, P.-L., et al.: Effective radiative forcing of anthropogenic aerosols in E3SM version 1: historical changes, causality, decomposition, and parameterization sensitivities, Atmospheric Chemistry and Physics, 22, 9129–9160, 2022.

455   Zhang, L., Michelangeli, D. V., and Taylor, P. A.: Influence of aerosol concentration on precipitation formation in low-level, warm stratiform clouds, Journal of aerosol science, 37, 203–217, 2006.